

Mantle flow geometry from ridge to trench beneath the Gorda-Juan de Fuca plate system

Robert Martin-Short, Richard M Allen, Ian Bastow, Eoghan Totten, Mark Richards

S1: Table showing the stacked splitting results for each station, along with the orientation angle (measured clockwise from North to the BH1 component) where applicable. The stations are color-coded according to their phase of deployment.

Cascadia initiative Phase 1 (2011-2012)

Station ID	Longitude	Latitude	Splitting fast axis [phi]	Splitting delay time [dt]	Station rotation (degrees)	Number of stacked events	95 % confidence interval [phi]	95 % confidence interval [dt]
FN18A	-124.7248	46.6998	-81.0	0.7	296.0	3	-106.0 to -50.0	0.3 to 1.3
J35A	-126.2668	45.4989	47.0	1.7	202.0	3	30.0 to 55.0	1.5 to 1.9
FN16A	-125.5161	46.7996	89.0	2.6	201.0	2	83.0 to 91.0	2.4 to 2.7
G03A	-126.1625	40.0591	-39.0	2.1	154.0	2	-56.0 to -30.0	1.4 to 2.9
J50A	-125.2991	46.6402	-57.0	2.6	93.0	4	-65.0 to -32.0	2.0 to 2.8
J33A	-124.5708	45.1066	73.0	1.4	12.0	2	63.0 to 87.0	0.9 to 1.8
J37A	-127.9853	45.8642	-57.0	0.7	264.0	1	-81.0 to -40.0	0.6 to 1.0
J54A	-128.8116	47.3358	55.0	1.4	27.0	3	49.0 to 61.0	1.2 to 1.6
J65A	-125.1396	47.8913	65.0	1.2	51.0	1	61.0 to 73.0	0.9 to 1.5
J63A	-130.0033	48.2065	-63.0	2.2	165.0	1	-75.0 to -56.0	1.7 to 2.6
J06A	-128.8010	43.2515	-31.0	1.3	225.0	2	-50 to -23.0	0.8 to 1.5
J41A	-124.5372	45.8119	75.0	2.4	60.0	3	65.0 to 89.0	1.6 to 3.1
M08A	-124.8953	44.1187	47.0	1.4	8.0	2	28.0 to 68.0	0.8 to 1.7
J28A	-127.1564	45.0636	51.0	1.5	206.0	1	15.0 to 60.0	0.4 to 2.5
J51A	-126.1641	46.7970	41.0	1.7	133.0	2	28.0 to 53.0	1.1 to 2.2
J61A	-128.1972	47.8725	75.0	2.5	257.0	4	56.0 to 87.0	2.1 to 2.7
J31A	-129.6727	45.5531	71.0	1.8	5.0	1	62.0 to 86.0	1.3 to 2.4
J55A	-129.7076	47.5305	-57.0	1.1	211.0	2	-71.0 to -49.0	0.8 to 1.4
J30A	-128.9069	45.4242	65.0	1.6	69.0	2	48.0 to 88.0	0.7 to 2.6
J68A	-127.8292	48.4810	73.0	1.0	158.0	3	65.0 to 81.0	0.8 to 1.4
J36A	-127.1225	45.6855	-51.0	2.0	37.0	1	-60.0 to -46.0	1.6 to 2.3
J43A	-126.1721	46.1378	79.0	1.7	82.0	2	74.0 to 86.0	1.4 to 2.0
J38A	-128.8531	46.0395	75.0	1.3	101.0	2	68.0 to 84.0	1.2 to 1.9
M07A	-125.1168	44.8988	-69.0	1.5	118.0	1	-96.0 to -49.0	1.0 to 2.1
J25A	-124.6216	44.4729	59.0	2.3	145.0	2	46.0 to 71.0	1.6 to 2.6
J44A	-127.0390	46.3230	-85.0	1.4	207.0	1	-110.0 to -79.0	1.2 to 1.8
J46A	-128.7883	46.6639	71.0	0.8	254.0	3	63.0 to 81.0	0.4 to 1.3
J42A	-125.2997	45.9331	79.0	2.1	83.0	2	76.0 to 82.0	1.8 to 2.3

M01A	-126.7221	49.1504	-79.0	2.2	100.0	3	-95.0 to -71.0	1.5 to 2.5
J45A	-127.9049	46.5209	59.0	0.6	12.0	2	50.0 to 65.0	0.4 to 1.0
M03A	-126.1040	47.8883	53.0	1.3	161.0	1	45.0 to 72.0	0.8 to 2.0
J59A	-126.4153	47.5096	53.0	2.1	109.0	1	43.0 to 57.0	1.6 to 2.4
J67A	-127.0842	48.1500	47.0	1.7	138.0	2	40.0 to 54.0	1.4 to 1.9
J29A	-128.0084	45.1757	-83.0	1.1	74.0	1	-92.0 to -78.0	0.9 to 1.3
J39A	-129.6441	46.1760	-3.0	1.3	323.0	3	-18.0 to 7.0	0.9 to 1.4
FN07A	-124.7865	46.8555	47.0	0.8	118.0	1	10.0 to 75.0	0.4 to 1.4

Cascadia Initiative Phase 2 (2012-2013)

Station ID	Longitude	Latitude	Splitting fast axis [phi]	Splitting delay time [dt]	Station rotation (degrees)	Number of stacked events	95 % confidence interval [phi]	95 % confidence interval [dt]
FS04B	-124.5097	40.2447	-75.0	2.0	151.0	1	-83.0 to -67.0	1.5 to 2.4
G30B	-128.3187	41.9551	-57.0	1.2	230.0	1	-73.0 to -52.0	0.9 to 1.4
G09B	-124.7187	40.6568	71.0	1.2	220.0	2	63.0 to 80.0	0.8 to 1.4
J63B	-130.0033	48.2064	-61.0	2.5	145.0	1	-72.0 to -58.0	2.0 to 2.9
FS02B	-124.7980	40.3511	77.0	2.1	78.0	5	70.0 to 80.0	1.9 to 2.4
G05B	-127.7480	40.0696	-67.0	0.8	231.0	2	-78 to -60.0	0.5 to 1.8
G20B	-126.6137	41.2993	-57.0	1.0	3.0	6	-73.0 to -38.0	0.5 to 1.6
G11B	-126.3781	40.6859	-75.0	1.7	39.0	2	-87.0 to -59.0	1.1 to 2.1
G03B	-126.1627	40.0592	-41.0	1.0	29.0	2	-61.0 to -25.0	0.5 to 1.5
G22B	-128.2751	41.3075	-65.0	0.8	260.0	3	-82.0 to -60.0	0.3 to 1.5
G34B	-125.2010	42.5554	-65.0	2.2	151.0	4	-71.0 to -57.0	1.6 to 2.5
M12B	-124.9461	42.1840	-67.0	1.6	235.0	2	-77.0 to -64.0	1.3 to 1.9
G17B	-124.3446	41.2839	53.0	1.9	87.0	2	40.0 to 71.0	1.4 to 2.2
J18B	-125.4660	44.0083	57.0	0.9	80.0	2	43.0 to 66.0	1.4 to 2.5
J20B	-127.0952	44.3542	57.0	1.0	331.0	3	26.0 to 70.0	0.4 to 1.8
G13B	-128.0289	40.6826	-83.0	1.3	225.0	2	-94.0 to -70.0	0.9 to 1.7
G28B	-126.7339	41.9428	-65.0	0.8	23.0	2	-85.0 to -53.0	0.5 to 1.3
FS09B	-124.8075	40.4369	-45.0	2.6	349.0	1	-53.0 to -43.0	2.0 to 3.0
M11B	-125.0171	42.9320	49.0	1.2	201.0	2	40.0 to 58.0	0.7 to 1.8
J06B	-128.8011	43.2515	-31.0	0.7	240.0	5	-61.0 to -18.0	0.2 to 1.3
J10B	-125.5435	43.3494	-89.0	1.9	89.0	2	-95.0 to -80.0	1.5 to 2.2
G18B	-124.9363	41.3016	-43.0	2.6	80.0	2	-51.0 to -42.0	2.2 to 2.8
J27B	-126.3074	44.8473	67.0	1.0	292.0	1	37.0 to 76.0	0.5 to 1.5
G21B	-127.4553	41.3167	-51.0	1.0	250.0	2	-75.0 to -38.0	0.5 to 1.2
FS01B	-124.9492	40.3268	-69.0	1.0	346.0	3	-79.0 to -63.0	0.7 to 1.3
G27B	-126.0167	41.9166	-89.0	1.0	212.0	3	-95.0 to -74.0	0.6 to 1.2
FS05B	-124.9001	40.3865	-77.0	2.8	307.0	1	-84.0 to -77.0	2.4 to 3.2
G25B	-124.5861	41.9199	71.0	2.0	334.0	2	66.0 to 74.0	1.8 to 2.3

G37B	-127.7213	42.5913	-63.0	1.1	102.0	6	-77.0 to -55.0	0.7 to 1.6
G02B	-125.2969	40.0486	-65.0	1.1	200.0	2	-72.0 to -60.0	0.9 to 1.2
G10B	-125.5533	40.6779	-77.0	1.4	133.0	4	-103.0 to -58.0	1.1 to 2.0
G35B	-126.0534	42.5677	-53.0	2.4	333.0	2	-67.0 to -41.0	1.8 to 2.8
J48B	-130.6395	47.1278	-65.0	1.4	201.0	2	-79.0 to -54.0	1.5 to 2.4
M14B	-124.5897	40.9850	49.0	2.0	266.0	1	43.0 to 57.0	1.5 to 2.5
J19B	-126.2705	44.1785	75.0	1.1	125.0	2	70.0 to 84.0	0.8 to 1.4
J09B	-124.7271	43.1510	89.0	2.4	163.0	1	80.0 to 93.0	1.8 to 3.0
G29B	-127.4834	41.9765	-61.0	1.2	329.0	4	-73.0 to -54.0	0.9 to 1.4
J23B	-129.6829	44.8442	-79.0	2.2	315.0	1	-90.0 to -70.0	1.9 to 2.4
M09B	-125.0589	44.2497	47.0	0.9	98.0	2	21.0 to 71.0	0.5 to 1.8
FS12B	-124.5059	40.4371	37.0	2.8	25.0	1	-4.0 to 70.0	1.2 to 3.1
FS20B	-125.0311	40.3896	65.0	1.1	0.0	3	56.0 to 72.0	0.6 to 1.5
G36B2	-126.9038	42.6000	-55.0	0.6	195.0	4	-58.0 to -43.0	0.3 to 0.9
J11B	-126.3677	43.5405	47.0	1.3	321.0	2	35.0 to 54.0	0.8 to 1.8
G19B	-125.7722	41.3081	-61.0	0.7	79.0	2	-78.0 to -30.0	0.2 to 1.0

Cascadia Initiative Phase 3 (2013-2014)

Station ID	Longitude	Latitude	Splitting fast axis [phi]	Splitting delay time [dt]	Station rotation (degrees)	Number of stacked events	95 % confidence interval [phi]	95 % confidence interval [dt]
J65C	-125.1394	47.8914	20.0	1.2	109.0	1	2.0 to 30.0	0.5 to 1.8
M03C	-126.1033	47.8881	44.0	2.2	327.0	3	12.0 to 50.0	1.8 to 2.2
J53C	-127.9209	47.1661	-77.0	1.0	301.0	5	-85.0 to -67.0	0.7 to 1.3
J25C	-124.6214	44.4722	-73.0	2.4	215.0	1	-85.0 to -61.0	1.6 to 3.0
M05C	-124.9357	46.1747	83.0	1.7	194.0	5	66.0 to 95.0	1.2 to 2.1
M01C	-126.7219	49.1498	39.0	0.7	138.0	2	20.0 to 45.0	0.5 to 1.4
J61C	-128.1964	47.8699	63.0	1.2	173.0	8	59.0 to 69.0	0.5 to 1.6
J52C	-127.0152	46.9907	21.0	0.3	129.0	7	5.0 to 32.0	0.0 to 0.6
J69C	-128.7386	48.6270	-89.0	2.2	37.0	3	-94.0 to -83.0	2.0 to 2.4
J26C	-125.4653	44.6534	53.0	1.5	63.0	1	47.0 to 60.0	1.2 to 1.7
J36C	-127.1252	45.6865	51.0	1.5	33.0	3	44.0 to 52.0	1.1 to 2.2
J32C	-130.6030	45.7145	-71.0	1.3	97.0	2	-85.0 to -49.0	1.0 to 1.6
J47C	-129.7139	46.8440	-47.0	0.8	219.0	3	-57.0 to -35.0	0.4 to 1.5
J52C	-127.0152	46.9907	55.0	1.7	129.0	1	47.0 to 60.0	1.1 to 2.4
J43C	-126.1725	46.1370	69.0	1.2	118.0	3	60.0 to 76.0	1.0 to 1.5
J50C	-125.2988	46.6411	45.0	2.0	339.0	1	40.0 to 51.0	1.7 to 2.3
M01C	-126.7219	49.1498	48.0	1.7	138.0	1	39.0 to 55.0	1.3 to 2.0
J63C	-130.0053	48.2047	-71.0	2.8	100.0	2	-82.0 to -62.2	2.4 to 3.1
J67C	-127.0868	48.1510	33.0	1.0	178.0	4	13.0 to 55.0	0.2 to 1.3

FN09C	-124.8872	46.8402	-75.0	2.5	162.0	2	-81.0 to -66.0	2.2 to 2.7
FN12C	-125.1190	46.8887	55.0	2.1	318.0	1	35.0 to 64.0	1.8 to 2.6
FN05C	-124.6556	46.8575	-77.0	2.1	357.0	1	-79.0 to -62.0	1.2 to 2.6
J35C	-126.2683	45.4995	49.0	2.0	333.0	3	32.0 to 58.0	1.4 to 2.5
J45C	-127.9048	46.5209	-61.0	0.9	109.0	3	-72.0 to -49.0	0.7 to 1.1
M05C	-124.9357	46.1747	59.0	1.1	194.0	1	50.0 to 71.0	0.5 to 1.6
J21C	-128.0376	44.5342	81.0	1.2	42.0	2	73.0 to 92.0	0.6 to 1.3
J44C	-127.0407	46.3240	-81.0	1.4	303.0	3	-92.0 to -73.0	1.0 to 1.8
J37C	-127.9850	45.8635	59.0	0.9	228.0	3	50.0 to 67.0	0.5 to 1.2
J23C	-129.6810	44.8438	55.0	1.0	147.0	2	31.0 to 73.0	0.5 to 1.3
J31C	-129.6724	45.5519	-71.0	1.6	234.0	2	-75.0 to -62.0	1.0 to 2.0
M06C	-124.9261	45.5287	65.0	2.0	359.0	1	40.0 to 71.0	1.5 to 2.4
J29C	-128.0085	45.1759	73.0	0.5	59.0	5	61.0 to 80.0	0.0 to 0.9
FN10C	-124.9935	46.8981	61.0	1.2	245.0	2	47.0 to 70.1	0.8 to 1.7
J39C	-129.6438	46.1761	31.0	1.0	268.0	3	10.0 to 46.0	0.3 to 1.2

Transportable Array Cascadia Sites (2010-2012)

Station ID	Longitude	Latitude	Splitting fast axis [phi]	Splitting delay time [dt]	Station rotation (degrees)	Number of stacked events	95 % confidence interval [phi]	95 % confidence interval [dt]
D04D	-122.7720	47.1786	59.0	2.2	NA	8	51.0 to 68.0	1.8 to 2.5
B05D	-122.0960	48.2641	-79.0	0.6	NA	16	-89.0 to -70.0	0.3 to 0.9
G05D	-121.3170	45.2422	79.0	1.5	NA	17	68.0 to 88.0	1.0 to 2.0
M04C	-121.8390	41.7826	65.0	1.2	NA	20	54.0 to 76.0	0.8 to 1.5
I03D	-123.3490	43.6972	63.0	1.5	NA	13	56.0 to 69.0	1.2 to 1.8
C06D	-120.8940	47.9229	71.0	1.4	NA	15	60.0 to 79.0	0.3 to 1.7
I05D	-121.3400	44.3386	79.0	1.5	NA	17	73.0 to 84.0	1.2 to 1.8
M02C	-122.8540	41.3920	71.0	1.1	NA	11	62.0 to 80.0	0.8 to 1.3
L02D	-123.6030	42.1578	65.0	1.2	NA	10	57.0 to 71.0	0.9 to 1.5
O03D	-121.8020	40.2947	-3.0	1.5	NA	5	-20.0 to 17.0	1.0 to 1.8
F05D	-121.4600	45.8852	83.0	1.1	NA	6	64.0 to 100.0	0.7 to 1.4
J04D	-122.1090	43.2405	65.0	1.5	NA	13	59.0 to 71.0	1.3 to 1.7
K02D	-123.6650	42.6955	49.0	1.5	NA	5	43.0 to 54.0	1.3 to 1.6
A04D	-122.7060	48.7201	85.0	0.8	NA	16	76.0 to 93.0	0.5 to 1.1
D03D	-123.0890	47.5347	85.0	1.3	NA	11	72.0 to 97.0	0.6 to 1.6
I02D	-123.8470	44.1059	63.0	1.0	NA	6	55.0 to 73.0	0.4 to 1.4
I04A	-122.4110	43.7941	61.0	1.6	NA	12	57.0 to 64.0	1.3 to 1.7
E04D	-122.5670	46.5566	79.0	1.3	NA	18	67.0 to 93.0	0.9 to 1.6
H04D	-122.7380	44.5234	59.0	1.9	NA	11	53.0 to 64.0	1.6 to 2.2
O02D	-122.7880	40.1766	33.0	0.7	NA	7	18.0 to 50.0	0.3 to 1.0
J01D	-123.9310	43.1614	65.0	1.9	NA	6	54.0 to 77.0	1.3 to 1.9

N02D	-122.7050	40.9740	75.0	0.7	NA	13	64.0 to 87.8	0.4 to 1.0
F04D	-123.0110	46.0829	77.0	1.1	NA	11	68.0 to 84.0	0.8 to 1.4
G03D	-123.2640	45.2115	85.0	1.6	NA	17	75.0 to 97.0	1.0 to 2.2
J05D	-121.2350	43.2848	77.0	1.8	NA	7	75.0 to 98.0	1.5 to 2.1
K04D	-121.7540	42.6246	75.0	1.6	NA	14	65.0 to 85.0	1.2 to 1.9
L04D	-122.3046	42.2180	57.0	1.5	NA	14	45.0 to 67.0	1.0 to 1.8

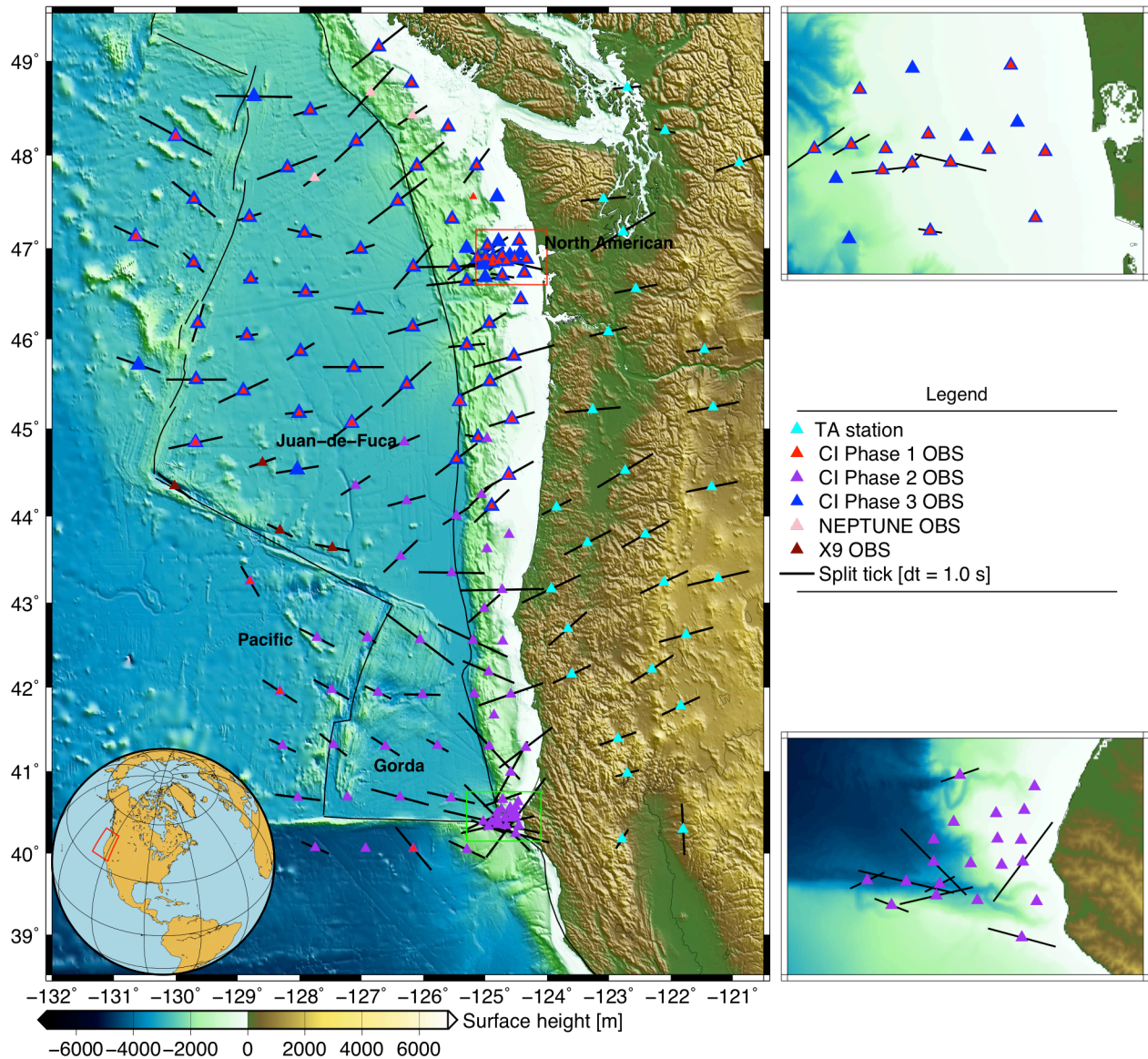
Network X9 (2013-2014)

Station ID	Longitude	Latitude	Splitting fast axis [phi]	Splitting delay time [dt]	Station rotation (degrees)	Number of stacked events	95 % confidence interval [phi]	95 % confidence interval [dt]
BB130	-127.4710	43.6388	71.0	0.6	244.0	4	61.0 to 95.0	0.2 to 1.2
BB300	-128.3180	43.8398	-23.0	0.6	298.0	4	-28.0 to -4.0	0.2 to 0.8
BB480	-130.0210	44.3489	-87.0	1.4	63.0	2	-101.0 to -71.0	1.0 to 1.6
BB330	-128.6000	44.6145	71.0	0.4	69.0	3	63.0 to 88.0	0.0 to 1.3

NEPTUNE broadband stations (2010-2014)

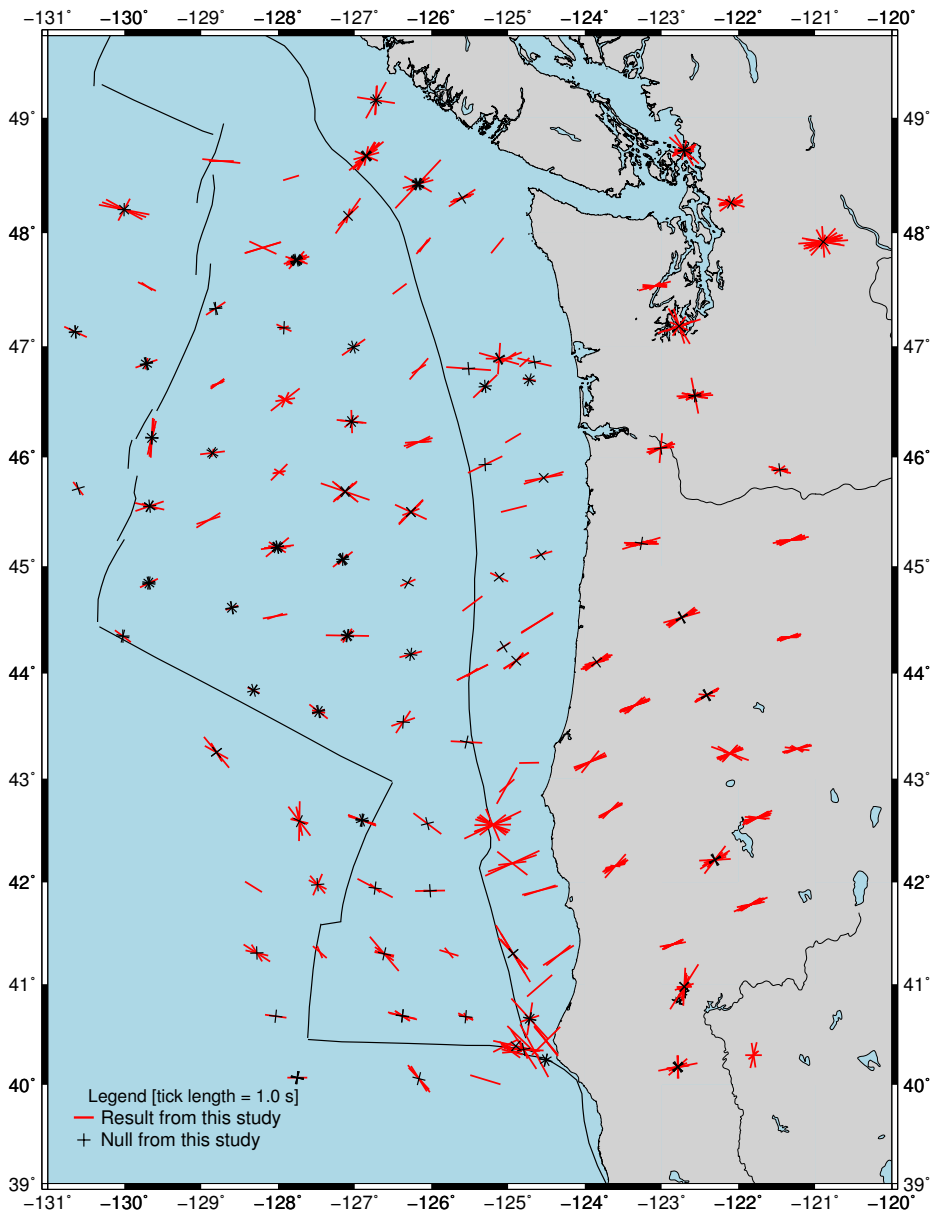
Station ID	Longitude	Latitude	Splitting fast axis [phi]	Splitting delay time [dt]	Station rotation (degrees)	Number of stacked events	95 % confidence interval [phi]	95 % confidence interval [dt]
NC27	-127.7580	47.7623	53.0	0.8	NA	20	40.0 to 73.0	0.5 to 1.2
NCBC	-126.1750	48.4275	57.0	1.0	NA	10	42.0 to 81.0	0.3 to 1.4
NC89	-126.8490	48.6705	43.0	1.9	NA	12	32.0 to 57.0	1.2 to 2.3

S2: Map showing the splitting results and the locations of the station deployments



S2A: This map shows all seismic stations deployed as part of Cascadia Initiative during phases 1 through 3 in addition to the X9 and NEPTUNE array seismometers used in this study. Black split ticks are plotted at all stations that produced one or more useable splitting result. Those stations not marked by a split tick either experienced technical problems or did not yield splitting results of sufficient quality.

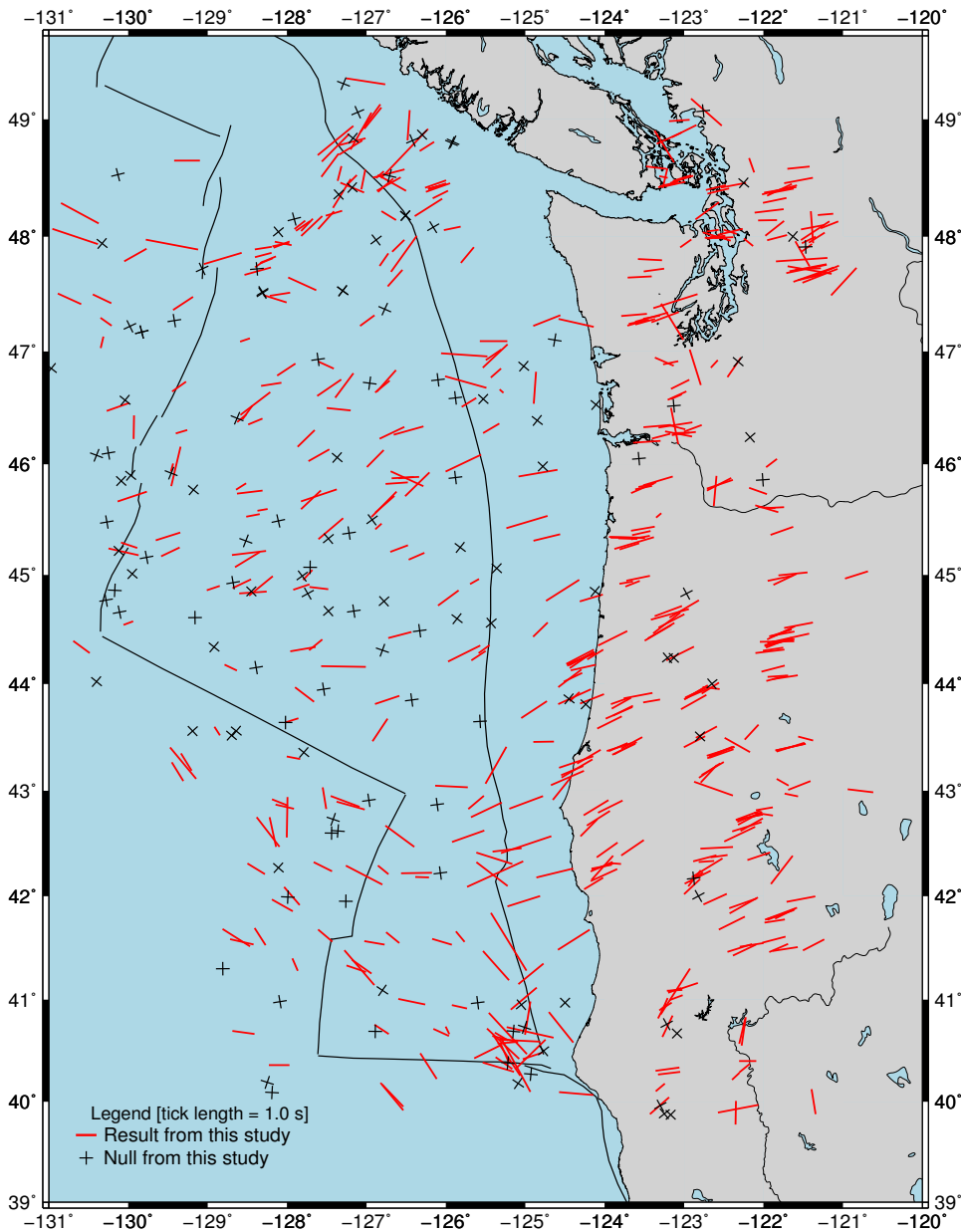
S3: Additional splitting maps showing all results included in the stacking



S3A: This map shows all individual splitting results used in the stacking process plotted at the surface. The number of measurements at each OBS instrument is typically low, and some stations exhibit wide range of splitting directions. This could be due to the influence of multiple layers of anisotropy, although it is currently not possible to test this hypothesis due to the limited backazimuthal distribution of the events we used.

Black crosses, whose two arms point in the backazimuth direction and at 90 degrees to it, indicate nulls. Null measurements occur either where the anisotropy is very weak, or when the LPO is

aligned either parallel or perpendicular to the initial polarization of the wave¹. This study uses only SKS and SKKS phases, which are assumed to be polarized in the backazimuth direction before they enter the anisotropic layer². Thus, a null result implies either that the anisotropic fast direction lies in parallel or perpendicular to the backazimuth, or alternatively that the anisotropy is weak¹. When present along with non-null results at the same station, nulls can be used to constrain the splitting geometry. However, nulls cannot be used to constrain delay times, so care must be taken when such results are included in the stacking procedure¹. See S6 for more detail.



S3B: This map shows all individual results used in the stacking process plotted at a piercing depth of 200km. Because the path taken by SKS and SKKS phases through the mantle to the seismometer

it not exactly vertical, each splitting measurement plots in a unique position. The anisotropic geometry indicated by this map is clearly complicated, but it displays the same regional pattern as inferred from the stacked maps such as figure 1. In some locations, wide ranges of splitting directions are seen to occur within a small area. This could be indicative of multiple layers of anisotropy. The abrupt change in FSD along the trench axis close to the Mendocino triple junction is a good example, and points to a complicated mantle flow situation. However, the short deployment time of the OBS devices and limited backazimuthal coverage of measurements obtained at each one makes it extremely difficult to model this dataset with anything more than a single layer of anisotropy.

S4: Additional information about the orientation code and procedure

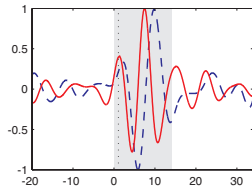
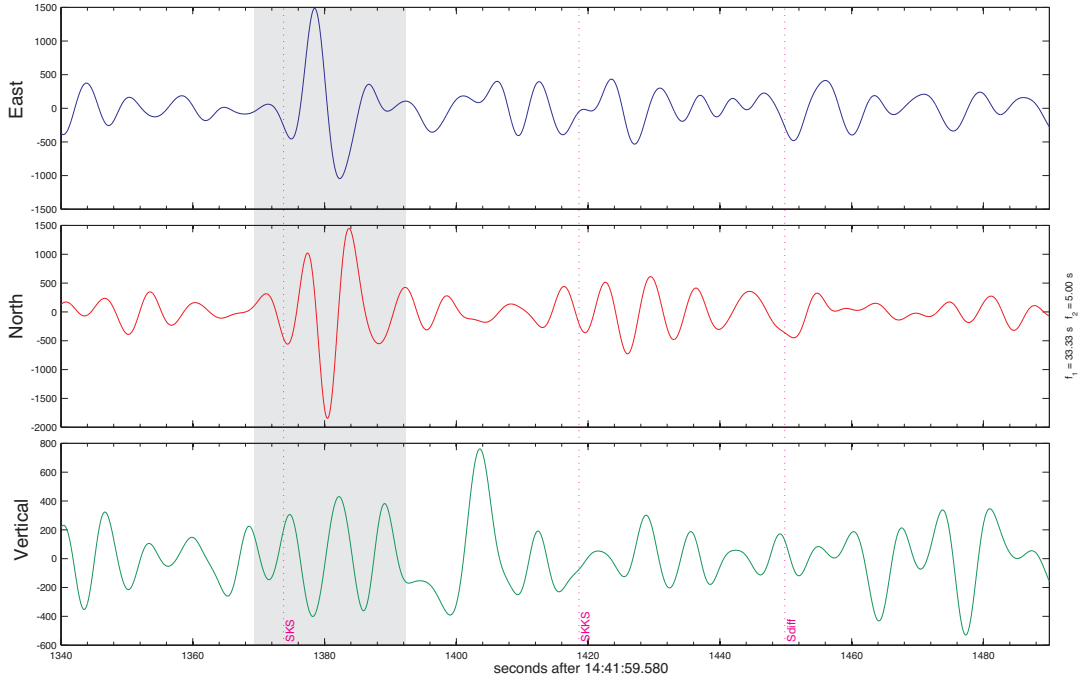
Full details of the Cascadia Initiative OBS deployments can be found in Lodewyk & Sumy³, who report site locations, instrument performance data and the horizontal orientation procedure. As described in this manuscript, the horizontal orientation code uses the Raleigh wave polarization method of Stachnik et al.⁴. The code was written by members of the Ocean Bottom Seismograph Instrument Pool (OBSIP) management office, and is freely available for download on their website (<http://www.obsip.org/data/obs-horizontal-orientation>). The accuracy of the code was verified by using it to estimate the orientation of the 27 onshore TA stations, which are known to have been precisely positioned so that their North and East components align with those directions³. Horizontal orientations for all Cascadia Initiative instruments were published by the OBSIP management office in a series of reports, which informed this study. Furthermore, we made use of the aforementioned code to determine new orientations for the five X9 OBS instruments used here. The three offshore instruments from the cabled NEPTUNE network were installed by submersible in the correct orientations and did not require use of the code⁵.

S5: Additional information about the choice of filter bands and the effects of filtering OBS data

A comparison between power spectral density (PSD) plots produced for the Cascadia Initiative stations and the high and low global noise models of Peterson⁶ provides an indication of how the offshore data performs relative to noise standards developed for land-based sites³. Probability density functions (PDFs) for horizontal channels are almost always above the high noise level, particularly in the microseismic bands and at longer periods

For the onshore data the optimal frequency band for splitting is in the region of 0.02-0.2Hz, which for the best events allows one to clearly see the SKS or SKKS arrivals (Figure S5a). The same frequency band is much less effective in the case of offshore data due to high levels of microseismic noise between 0.1 and 0.2 Hz. A compromise must thus be reached between the need to remove this noise and the need to preserve SKS energy; this is commonly achieved with a filter band of 0.05-0.15 Hz. However, it must be noted that in the case of the highest quality splitting, consistent values for the splitting parameters are obtained for a wide range of upper corner frequencies from 0.13 to 0.2 Hz. Furthermore, in the case of some station-event pairs the splitting result is degraded by lowering the upper corner frequency of the bandpass filter below about 0.15 Hz (Figure S5b).

Event: 10-Feb-2011, (041); Station: H04D; E65.8%
 $M_w = 6.5$ Backazimuth: 290.28° Distance: 104.11° Depth: 531km



Event: 10-Feb-2011 (041) 14:41 3.97N 123.12E 512km Mw=6.5
 Station: H04D Backazimuth: 290.2° Distance: 104.03°
 init.Pol.: 116.3° Filter: 0.050Hz - 0.20Hz SNR_{sc}: 9.4

Rotation Correlation:	43 <	63° <	86	1.7 <	2.1s <	2.5
Minimum Energy:	60 <	62° <	68	1.9 <	2.1s <	2.3
Eigenvalue:	58 <	66° <	80	1.9 <	2.1s <	2.3
Quality:	good	IsNull:	No	Phase:	SKS	

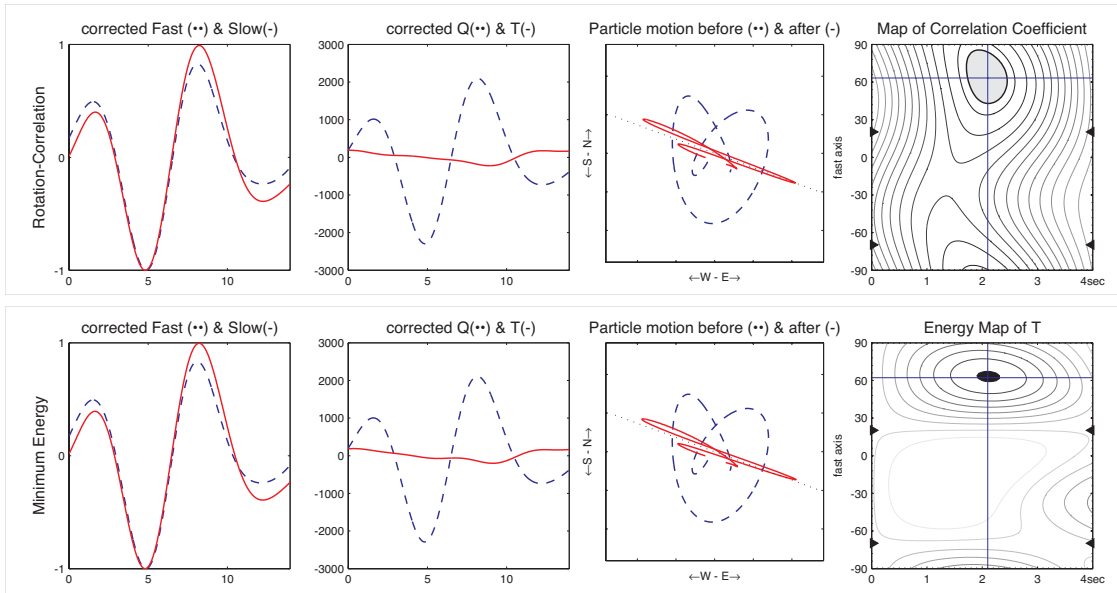
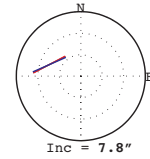
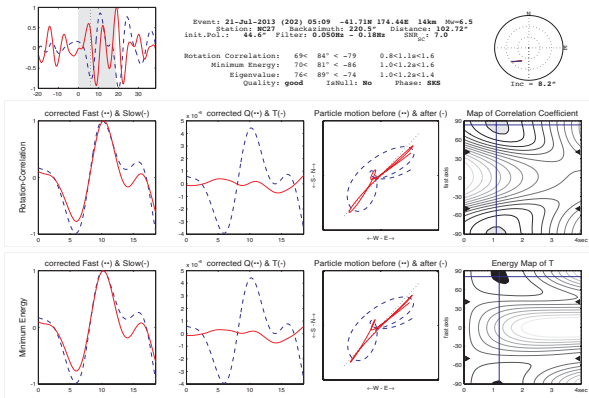
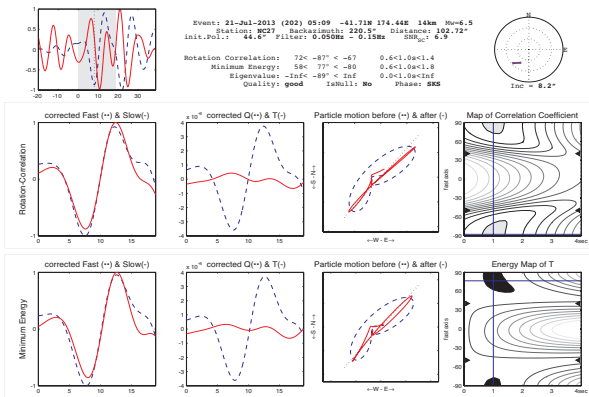


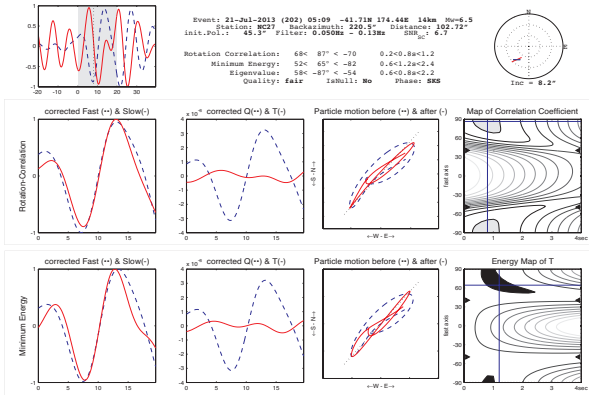
Figure S5a: These panels show an example of an excellent shear wave splitting result obtained using Splitlab with data from TA station H04D. The upper panel shows a zoom-in section of the data filtered at 0.02-0.2Hz. An SKS phase arrival is clearly seen in the horizontal components and is marked by a grey window. The lower panel shows the calculated splitting parameters: The waveforms in the upper-left corner at the uncorrected North and East components (or BH1 and BH2 in the case of OBS data). The central display of four plots shows the prediction of the rotation correlation (RC) method, while the lower display corresponds to the minimum energy (SC) method. Within each display the left-most plot shows the fast and slow phases identified by the program. The second plot from the left shows the corrected radial and transverse (red) components and the third shows the particle motion before and after the splitting correction. The goal of these shear wave-splitting methods is to incrementally rotate and time-shift the horizontal components so that the particle motion is linearized as far as possible. Thus the more linear the corrected motion, the higher quality the split. The fourth plot in each display shows a contour plot of the error matrix, with the colored area representing the 95% confidence interval. The smaller this region and the greater the agreement between the methods, the more confident we can be in the result.



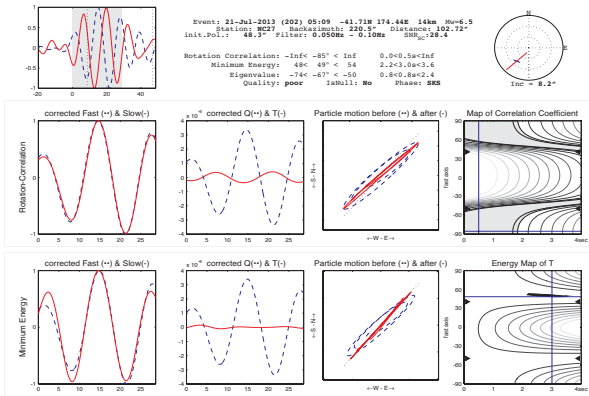
1) 0.05-0.18Hz



2) 0.05-0.15Hz



3) 0.05-0.13Hz



4) 0.05-0.10Hz

Figure S5b: Panels showing the effects of filtering on a good measurement obtained from NEPTUNE offshore station NC27. The SKS arrival for this particular event is very clear, and a high quality splitting measurement is obtained with a relatively large passband of 0.05-0.18 Hz. In the case of this event, lowering the upper corner frequency of the filter degrades the quality of the splitting result and makes the measurement look increasingly null (see Restivo & Helffrich⁷). This highlights the need to test a range of frequency bands when dealing with OBS data in order to ensure that the filtering process is not unduly removing signal energy.

S6: Additional information about null results and how they were dealt with

Null shear wave splitting measurements arise in isotropic media or where the seismic anisotropy is aligned either parallel or perpendicular to the initial polarisation of the incoming wave. This means that either the fast direction is equal to or 90 degrees from the initial polarization direction.

Since SKS and SKKS phases are assumed to be radially polarised when they enter the anisotropic layer, nulls should occur when the fast direction is parallel or perpendicular to the backazimuth¹. Thus, they can help to constrain the splitting direction at a station, but only when used with true splitting results for different events at that station.

Wustefeld & Bokelmann¹ note that in the case of a null measurement, the angular difference between the fast direction estimates of the SC and RC methods should be approximately an integer multiple of 45 degrees, and the delay time estimate of the RC method should be close to zero. This criteria in this study to identify and classify nulls (see figure S6a) and they were subsequently incorporated into the stacking process.

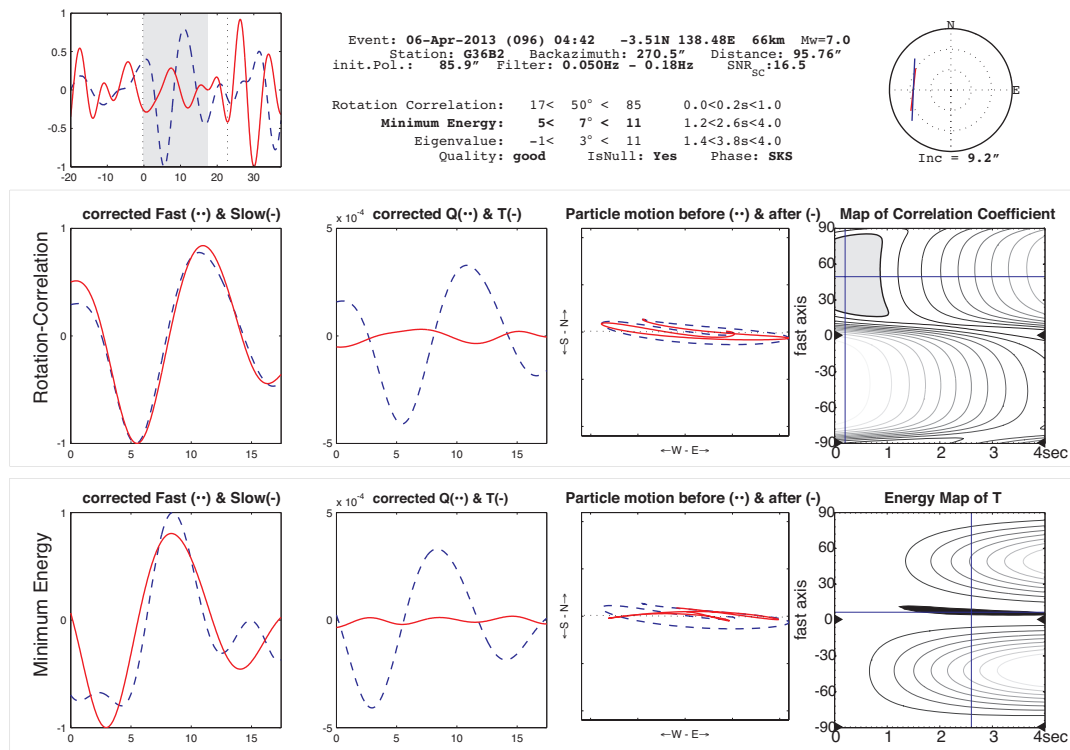


Figure S6a: This figure shows a typical null result for OBS station G36B2. Nulls occur when either the fast or slow axis and initial polarisation are almost equal, which means that the particle motion is well linearized before splitting correction. This result is classified as a good null because the angular difference between the SC and RC estimates is almost 45 degrees, the RC delay time estimate is almost zero and the signal to noise ratio is high. Null measurements must be treated with care because their delay time error range is generally high, but they can provide useful constraint on the splitting fast direction when combined with true splitting results and so are included in the stack.

S7: Notes on the well-constrained ridge-parallel results at site J39

The discovery of a well-constrained, approximately ridge-parallel splitting pattern at site J39 was unexpected and demanded further investigation to ensure that it was not the result of errors in instrument orientation or splitting window choice. Site J39 was occupied during phases 1 and 3 of the Cascadia Initiative and produced high quality results for both phases. Figure S7a shows examples of ‘good’ splits obtained from the site; the consistency in results between the two phases suggests a suitable level of accuracy in the station orientations and method of splitting parameter determination.

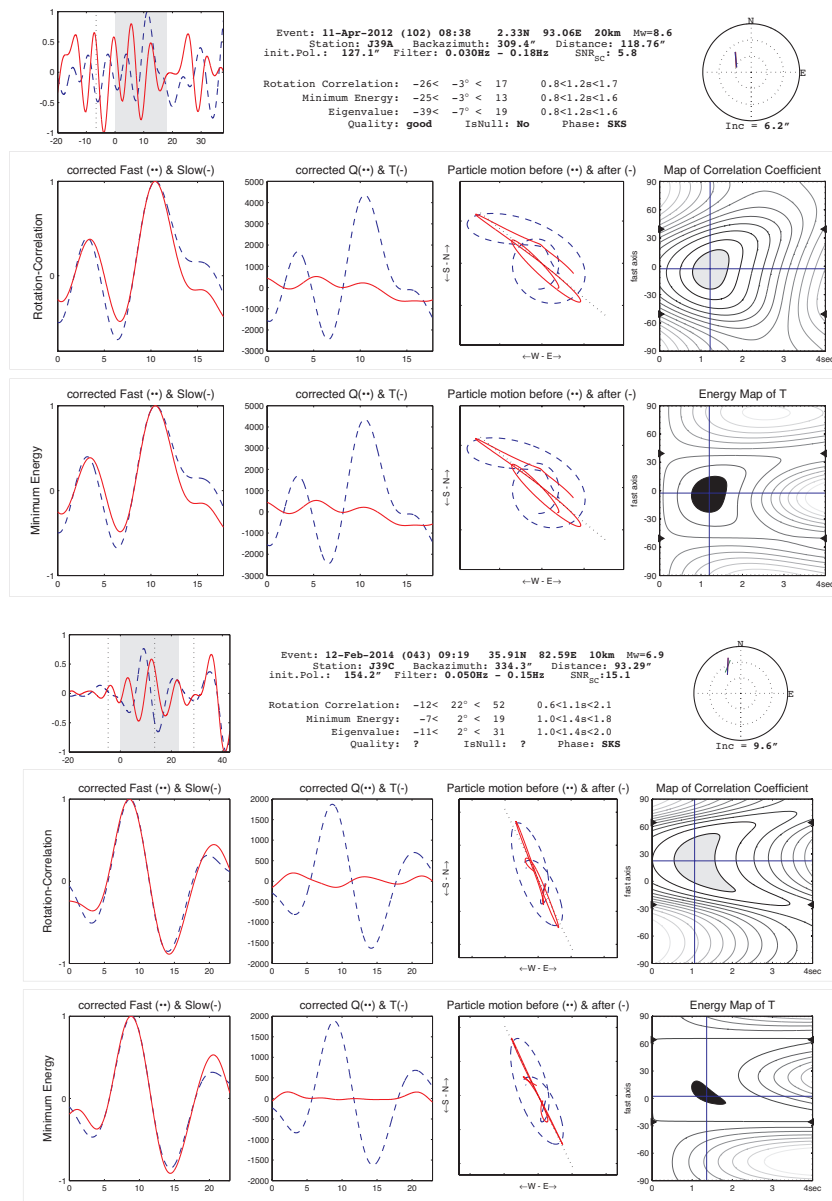


Figure S7a: Two high-quality splitting measurements from site J39, both of which indicate fast directions that lie sub-parallel to the ridge. The upper panel shows a measurement from station J39A (Cascadia Initiative phase 1), while the lower panel shows one from J39C (Cascadia Initiative phase 3). These results are both classified as good due to the close agreement between the spitting parameter estimates of the three methods, good particle linearization and a roughly 180 degree difference between the backazimuth and initial polarization directions, which indicates that the component orientation procedure produced an accurate result.

S8: Notes on the lack of correlation between splitting time and distance onshore of the trench to at least 400km

Currie et al⁸ observe a notable increase in splitting delay times with distance from the trench in their published dataset of 23 measurements from onshore stations situated in the Cascadia Forearc. They attribute this to the increasing influence of anisotropy in the mantle wedge, which thickens to the east. However, our much larger onshore dataset shows no correlation between delay time and distance from the trench out to a distance of 400km. This suggests that the mantle wedge probably provides minimal contribution to the splitting signal in this region.

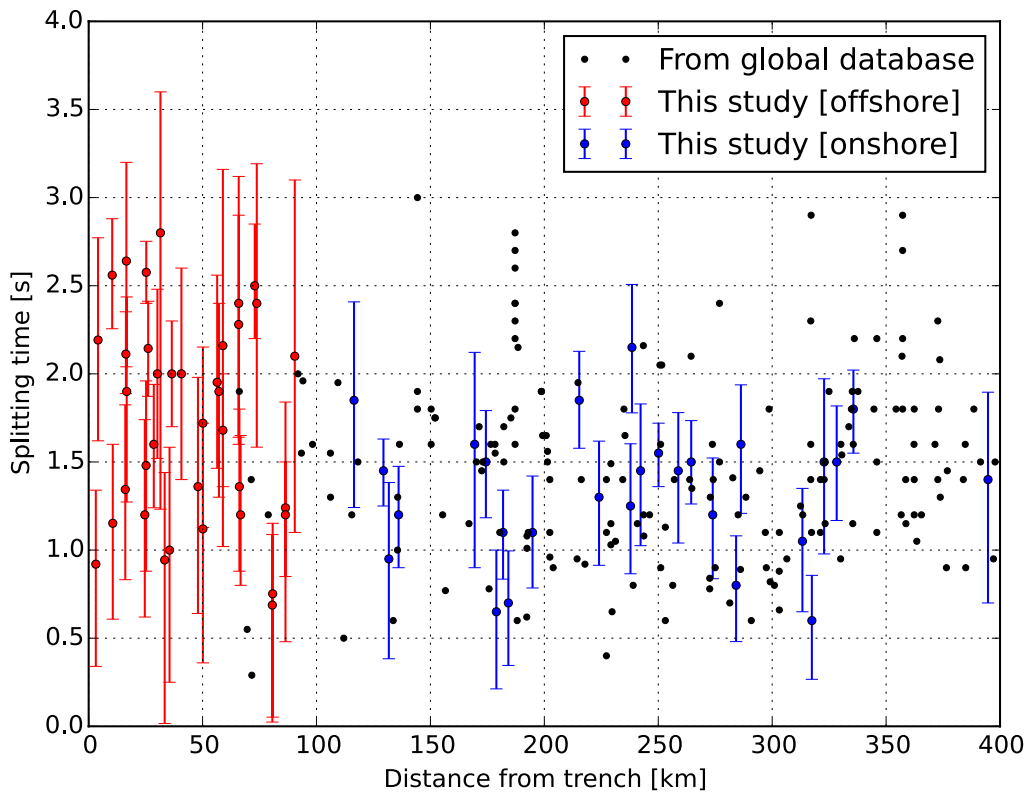


Figure S8a: Graph showing splitting delay times for all sites on the North American plate (East of the trench) plotted against distance from the trench. The graph displays results obtained in this study in addition to those recorded in the global database of Wustefeld et al.¹⁰. The error bars for

delay time measurements obtained from this study are very large in the case of the offshore stations, but are typically much smaller at the TA sites, reflective of the much lower noise levels present there. However, despite this, there is clearly no correlation between splitting delay time and distance out to 400km from the trench. Error bars correspond to the 95% confidence interval.

S9: Differentiation between the arcuate splitting patterns discussed by Eakin et al (2010) and Zandt & Humphreys (2008), and the interpretation of this study

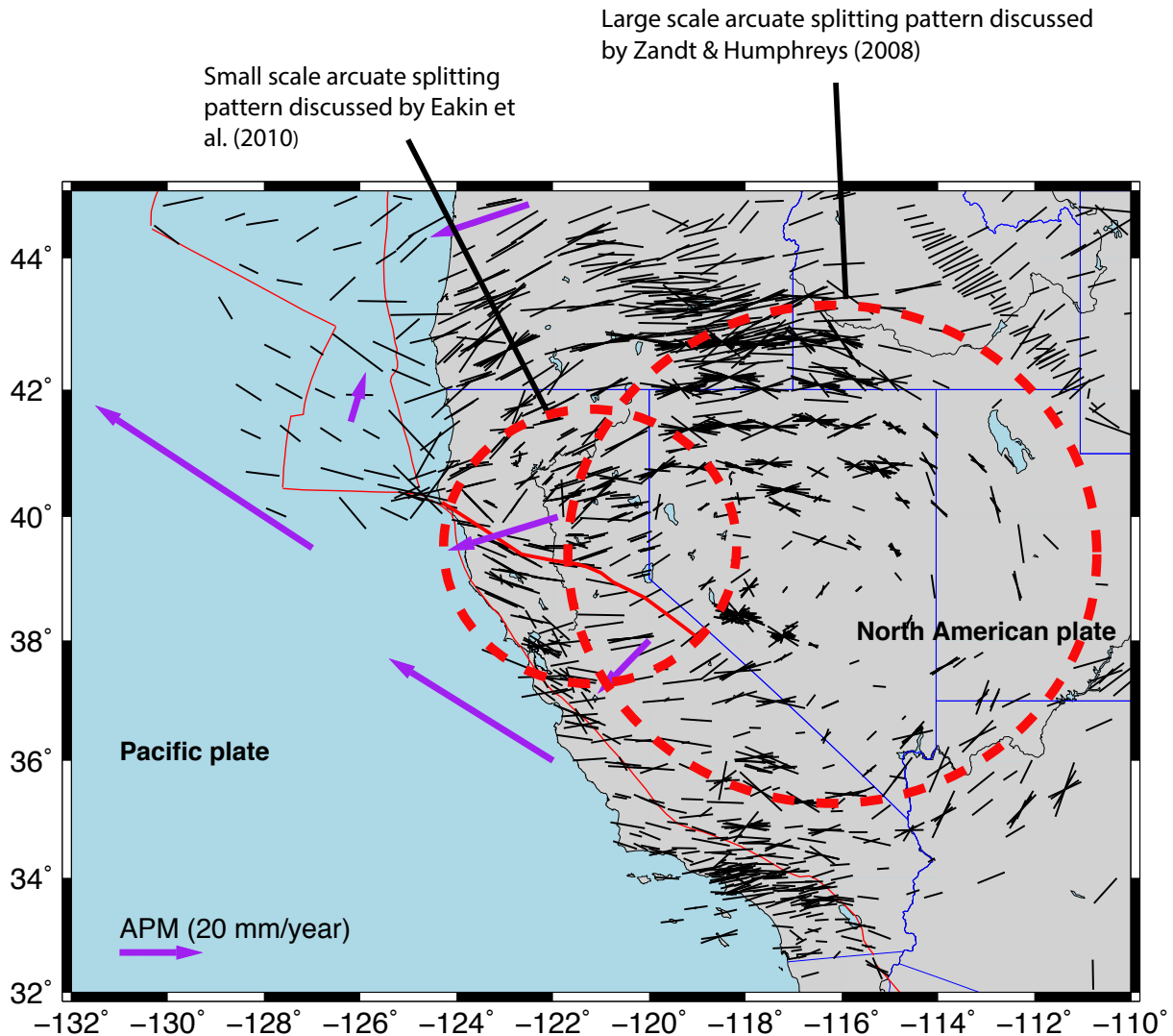
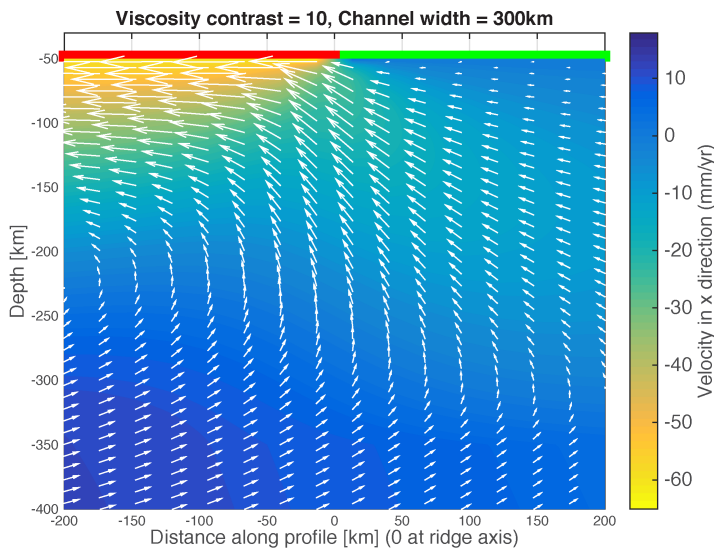


Figure S9a: This map highlights two arcuate splitting patterns observed near the edge of the downgoing Gorda slab. The first, a large-scale feature centred on Nevada, was interpreted to be the result of mantle flow around the edge of the slab by Zandt & Humphreys¹¹. Eakin¹² interpreted the second, a smaller scale pattern centred on Northern California, in the same fashion. Given our splitting observations on Gorda and the findings of our geodynamic model, we suggest that the

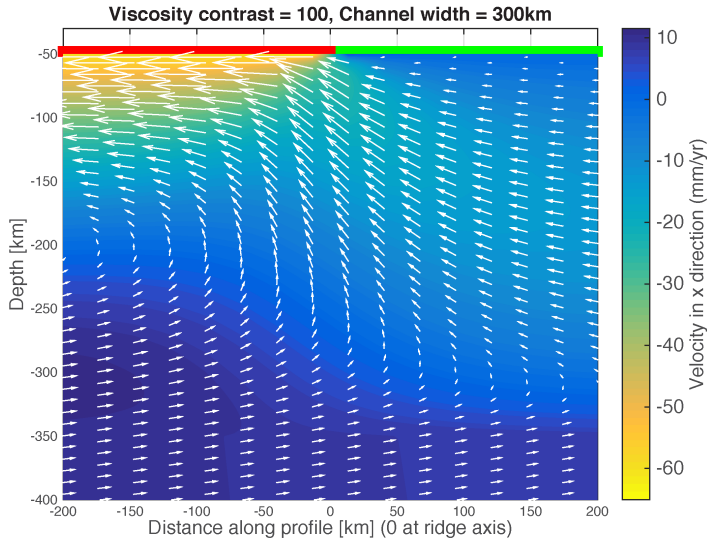
second, small-scale pattern could mainly be the result of Pacific plate motion. Indeed, there are likely two layers of mantle flow near the slab edge: One, a shallow asthenospheric flow influenced by the motion of the fast-moving Pacific plate and two, a deeper, actuate flow around the slab edge that is driven by rollback.

S10: Further results from geodynamic modelling of an asthenosphere of varying thickness and viscosity contrast.

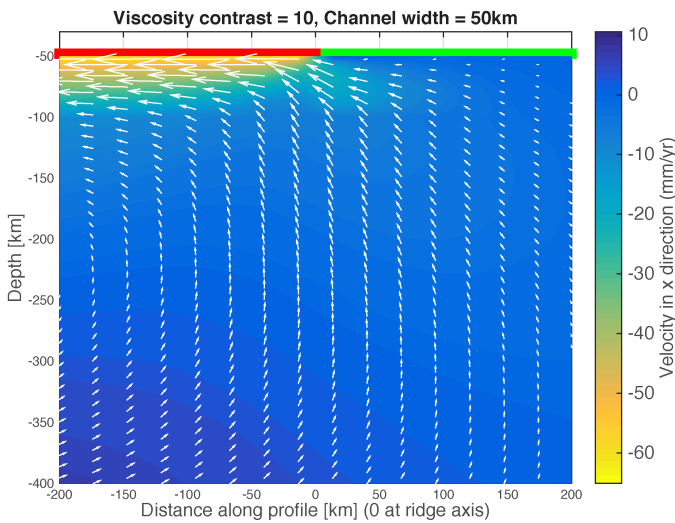
In this study we use the method of Hager and O’Connell¹³ to produce a simple, two-dimensional geodynamic model of mantle flow in section perpendicular to the Gorda ridge. Our preferred model features a two layer upper mantle, with a low viscosity asthenospheric channel of thickness 100km. However, we also varied the choice of asthenosphere thickness and velocity contrast in an effort to understand the range of flow geometries that could possibly exist. The flowing figures show four end-member cases, all of which suggest the existence of induced mantle flow beneath the Gorda plate.



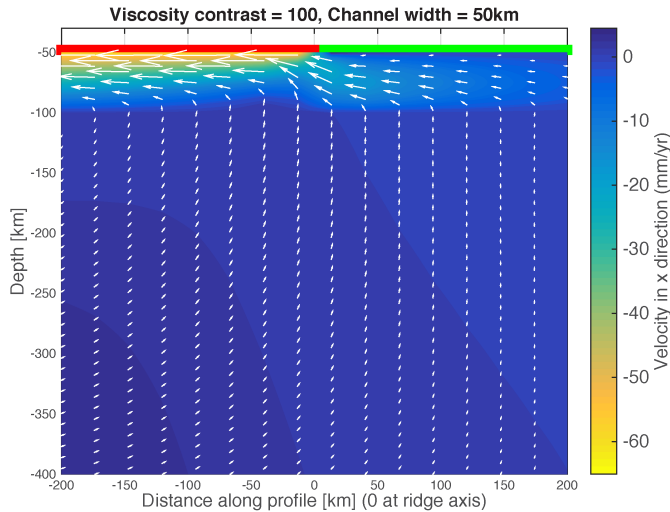
S10a: Model featuring a 300km thick asthenosphere underlain by a mesosphere of 10 times the viscosity. Westwards motion of the red plate induces a significant flow field throughout the model, including a dominantly westwards flow field below the stationary (green) plate.



S10b: Model featuring a 300km thick asthenosphere underlain by a mesosphere of 100 times the viscosity. The induced mantle flow field looks similar to that above, but velocities within the low viscosity channel are enhanced.



S10c: Induced mantle flow field in the case where the asthenosphere has thickness 50km and the underlying mesosphere has 10 times the viscosity. Motion of the red plate is still able to induce flow beneath the stationary green plate, but this is much reduced compared to the situation in S10A



S10d: Induced flow in an asthenosphere with thickness 50km and viscosity contrast of 100. The domain is dominated by flow in the low viscosity channel, which extends beneath the entirety of the green plate.

References in this document

- [1] Wüstefeld, A. & Bokelmann, G. Null detection in shear-wave splitting measurements. *Bull. Seis. Soc. Am* **97**, 1204-1211 (2007).
- [2] Vinnik, L. P., Farra, V., & Romanowicz, B. (1989). Azimuthal anisotropy in the Earth from observations of SKS at Geoscope and NARS broadband stations. *Bull. Seis. Soc. Am*, **79**, 1542-1558 (1989).
- [3] Lodewyk, J. & Sumy, D. Cascadia Amphibious Array Ocean Bottom Seismograph Horizontal Component Orientations. OBSIP Management Office (2014). At <http://www.obsip.org/experiments/experiment-list/2011/cascadia>
- [4] Stachnik, J. *et al.* Determination of New Zealand ocean bottom seismometer orientation via Rayleigh-wave polarization. *Seismol. Res. Lett.* **83**, 704-713 (2012).
- [5] Heesemann, M., Izsua, T. L., Scherwath, M., Juniper, S. K. & Moran, K. Ocean Networks Canada: From geohazards research laboratories to Smart Ocean Systems. *Oceanography* **27**, 151-153 (2014).
- [6] Peterson, J. Observations and modeling of seismic background noise. 93-95 (1993)
- [7] Restivo, A. & Helffrich, G. Teleseismic shear wave splitting measurements in noisy environments. *Geophys. J. Int.* **137**, 821-830 (1999).
- [8] Currie, C. A., Cassidy, J. F., Hyndman, R. D. & Bostock, M. G. Shear wave anisotropy beneath the Cascadia subduction zone and western North American craton. *Geophys. J. Int.* **157**, 341-353 (2004).

- [9] Karato, S., Jung, H., Katayama, I. & Skemer, P. Geodynamic significance of seismic anisotropy of the upper mantle: new insights from laboratory studies. *Annu. Rev. Earth Planet. Sci.* **36**, 59-95 (2008).
- [10] Wüstefeld, A., Bokermann, G., Barruol, G. & Montagner, J. Identifying global seismic anisotropy patterns by correlating shear-wave splitting and surface-wave data. *Phys. Earth Planet. Inter.* **176**, 198-212 (2009).
- [11] Zandt, G., and E. Humphreys. Toroidal mantle flow through the western US slab window. *Geology.* **36**, 295-298 (2008)
- [12] Eakin, C., *et al.* Seismic anisotropy beneath Cascadia and the Mendocino triple junction: Interaction of the subducting slab with mantle flow. *Earth. Planet. Sci. Lett.* **297** (3), 627-632 (2010)
- [13] Hager, B. & O'Connell, R. A simple global model of plate dynamics and mantle convection. *J. Geophys. Res.* **86**, 4843-4867 (1981).